Basic Concepts and Parameters of Astronomical AO Systems

S. Esposito and E. Pinna

INAF - Osservatorio Astrofisico di Arcetri, L.go E. Fermi n.5 - 50125 Firenze, ITALY
esposito@arcetri.astro.it

Abstract. The paper describes the basic concepts and parameters of astronomical adaptive optic (AO) systems. In particular, the paper introduces and discusses the main parameters and error sources that determine the performances of an AO system. From this discussion, the current limitations of AO systems are derived. Following this, the laser-generated reference star method is described, being the best technique to solve the main limitation of Astronomical AO system, namely the limited sky coverage. Then advantages and disadvantages of such technique are given. Using the considered matter, the case of LBT, the first 8 m class telescope using a deformable secondary mirror, is described. The LBT AO system performances in the single telescope case are briefly outlined. Then some concepts of optical interferometry are reported. They are used to analyze the definition of homothetic interferometer, the LBT case, and explain its differences from the Michelson stellar interferometer configuration. Finally a short description of the LBT interferometric instruments is given.

S. Esposito and E. Pinna: *Basic Concepts and Parameters of Astronomical AO Systems*, Lect. Notes Phys. **742**, 45–78 (2008)
DOI 10.1007/978-3-540-68032-1_3

Key words: Atmospheric wavefront aberration, Adaptive Optics, Laser Guide Star, Homotetic interferometer, Large Binocular Telescope

1 Introduction

High angular resolution observations became more and more important in modern Astrophysics in all the classical research fields from Solar System studies to Cosmology. In this framework, the development of techniques that allow us to reach diffraction limited performance using the present telescopes are of high importance. Among all the techniques applied to ground-based telescopes to reach a diffraction limited performance, the most powerful one is the so-called *Adaptive Optics* or AO. This technique aims to measure the wavefront perturbation due to refraction index fluctuations of the atmosphere and then to correct it quickly to follow the turbulence evolution. In this kind of system, there are three fundamental elements, as shown in Fig. 1; the wavefront sensor that measures the instantaneous wavefront aberration, the wavefront corrector that corrects the phase fluctuation introducing different optical paths for different rays, and the control system, or the so-called wavefront computer that computes from the wavefront sensor data the commands to be applied to the wavefront corrector. The wavefront corrector is usually

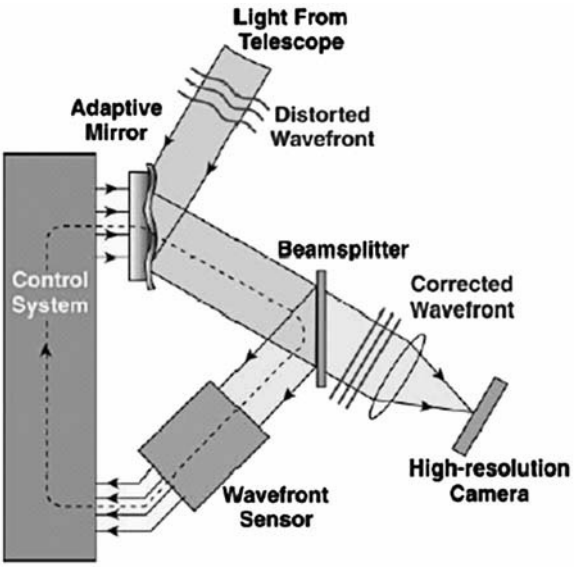

Fig. 1. A block diagram of an AO system. The figure reports the deformable mirror, the wavefront sensor, and the wavefront computer and highlights the two different optical paths of the light from the reference source and the scientific target, respectively

a deformable mirror[1]. Finally the system needs a reference star to measure the wavefront aberration. This object has to be quite bright as we will see in the next sections. Hence, in some cases it cannot be the scientific target itself because it is too dim. In this situation, the reference star has to be angularly close enough to the scientific target so that the achieved wavefront measurement can be successfully used to correct the image of the scientific object. The adaptive optics system having the architecture presented in Fig. 1 was introduced for the first time by H. Babcock in 1953 [1]. Following this, authors like Tatarsky [27] and Fried [10] developed the basis of the theory of image formation in random media, which has subsequently been directly applied to compute the performance and limitation of AO systems. The practical realization of an AO system in Astronomy began later, at the end of the 1980s, with the construction of the Come-On system [25] for the ESO 3.6 m telescope on La Silla. From then on, all the 8 m class telescopes like VLT, Keck, Gemini, Subaru, and LBT have built and planned many different types of AO systems. Today, the majority of professional telescopes of the 4 m and 8 m class have an adaptive optics system and related diffraction limited instruments.

This lecture can be divided in to two parts. The first part aims to describe the basic concepts and limitations of contemporary AO systems (Sects. 2,3,4,5, and 6). The second part (Sects. 7 and 8) briefly introduces the AO systems of LBT telescope [17] for the single telescope first and then in interferometric mode. Here, the aim is to describe what should be available in terms of angular resolution at LBT in the next few years. Also as optical interferometry is becoming increasingly important with time, we outline some basic features of interferometric beam combinations, in particular in relation to the concept of homothetic interferometers. Homothetic interferometers allow one to divide interferometers into two classes, the Michelson stellar interferometer b[22] (like the VLTI) and the Fizeau interferometers (like the LBT). It is clear that an AO system is now a fundamental sub-system of any instrument of an 8–10 m class telescope and indeed of any extremely large telescope (ELT) presently under design. Hence, we believe that it is crucial for the next generation of young astronomers to have a thorough knowledge of the basic principles of AO.

2 Opening Notes on Image Formation in Astronomical Telescopes

We will summarize in the following some basic results on image formation theory, as achieved following the linear theory of optics and Fourier Optics in particular. For the rest of the paper, we will consider all the astronomical objects as incoherent sources so that the superposition principle applies to

[1] By deformable mirror (DM), we mean an electro-optical device having a reflecting surface with an adjustable shape.

the object intensities and not to the object electric field. Having said that, we start our work from the basic equation reported below

$$I(\boldsymbol{\alpha}) = \int O(\boldsymbol{\beta})\mathrm{PSF}(\boldsymbol{\beta} - \boldsymbol{\alpha})\mathrm{d}\boldsymbol{\beta}, \tag{1}$$

where $\boldsymbol{d} = \lambda \boldsymbol{f}$ while $\boldsymbol{\alpha}$ and $\boldsymbol{\beta}$ are two bi-dimensional vectors giving the 2D coordinates of a point in the telescope focal plane expressed as angle, $O(\boldsymbol{\alpha})$ and $I(\boldsymbol{\alpha})$ are the object and image intensity distributions, respectively, $\mathrm{PSF}(\boldsymbol{\alpha})$ is the telescope's so-called Point Spread Function or the image of a point like source. This last quantity is easily determined using Fourier optics and can be expressed as:

$$\mathrm{PSF}(\boldsymbol{\alpha}) = \mid \mathrm{FT}\left[W(\boldsymbol{\alpha})\right] \mid^2 \tag{2}$$

In writing this equation, we assumed that no aberration is present and so the function W, the so-called telescope pupil function, is simply one inside the circle of radius R and zero outside[2]. For this circular aperture telescope, the PSF is usually called the Airy disk that has an FWHM equal to

$$\theta = \lambda / D,$$

where λ and D are the operating wavelength and the telescope diameter. A cut passing through the center of the PSF is represented in Fig. 2. The meaning of (1) can be clarified by looking at the same formula in the Fourier space, as is usually done in Fourier Optics. Taking the fourier transform of both members of (1), we obtain the following relationship

$$\widetilde{I}(\boldsymbol{f}) = \widetilde{O}(\boldsymbol{f}) \cdot \widetilde{P}(\boldsymbol{f}) \tag{3}$$

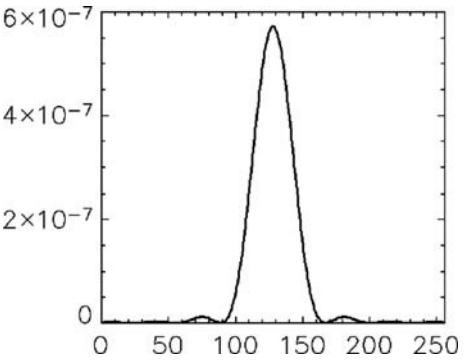

Fig. 2. The central cut of the Point Spread Function of a diffraction limited circular lens

[2] We will assume for all the following a circular telescope with no obstruction.

where $\boldsymbol{f}$ is the bidimensional coordinate in the Fourier plane, and P indicates now for simplicity the PSF function. Taking the modulus of left and right members of above equation gives:

$$| \widetilde{I}(\boldsymbol{f}) | = | \widetilde{O}(\boldsymbol{f}) | \cdot | \widetilde{P}(\boldsymbol{f}) | \tag{4}$$

The modulus of $\widetilde{P}$ is defined in optics as the Modulation Transfer Function (MTF) and can be expressed considering the equation for the PSF and the Fourier transform auto-correlation theorem in the following way:

$$\mathrm{MTF}(\boldsymbol{f}) \propto \int W(\boldsymbol{r}) W(\boldsymbol{r} + \lambda \boldsymbol{f}) \mathrm{d}\boldsymbol{r} \tag{5}$$

It is easy at this point to see that the MTF acts like a filter that attenuates (and de-phases) the Fourier components of the intensity distribution of the considered object. If the MTF is close to zero or zero at a given spatial frequency, that frequency will not be present in the object image. Moreover, it is clear to see that when $\lambda \boldsymbol{f} > D$ the MTF is zero so that the maximum spatial frequency transmitted by the telescope is D/λ. A graphical representation of the MTF can be found considering that the integral of (5) is given by the over-position area of the two circles of diameter D displaced by a quantity $f\lambda$, as reported in Fig. 3. In the case where no aberrations are present, the MTF function can be analytically derived. [The mathematical expression is quite complicated and can be found in several Optics textbooks [15].] However the diffraction-limited MTF behavior is very simple and almost linear, as reported in Fig. 4. In this case, it easy to see that the MTF retains a value different from zero for all the x axis values or all the spatial frequencies in the range $0, D/\lambda$. When some aberrations are present, the system MTF is degraded, and higher spatial frequencies are attenuated or no longer even transmitted.

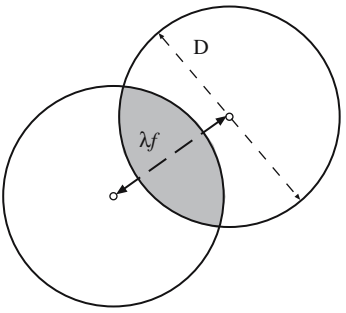

Fig. 3. The geometrical arrangement of the autocorrelation integral of (5). The frequency f here is an angular frequency so that $f\lambda$ is a length. The maximum f where the MTF is different from zero is clearly $f = D/\lambda$

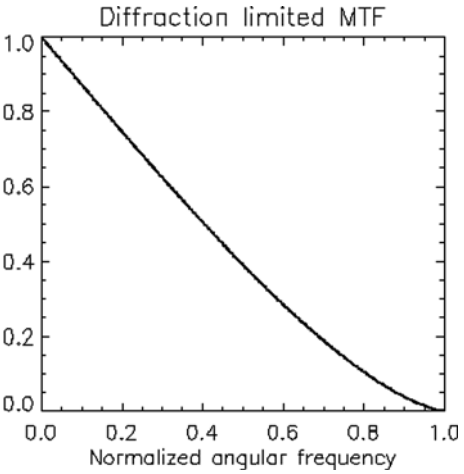

Fig. 4. The analytical representation of the MTF as function of angular frequency normalized at D/λ

3 Atmospheric Turbulence and Wavefront Aberrations

We mention in the introduction that the performance of ground-based telescopes is limited by the atmospheric refraction index fluctuations. Refraction index fluctuations originate when a turbulent flow of air is present. This turbulence, coupled with the fact that the atmospheric temperature is changing with altitude, creates a mix of air particles of different temperatures, which in turns generate the refraction index fluctuations. As we see, the wavefront passing through the atmosphere is disturbed or more precisely aberrated by these fluctuations. In this section, we will quantify the wavefront aberration due to atmospheric turbulence introducing the phase structure function and the Fried parameter r_0 starting from the velocity fluctuation in a turbulent flow.

3.1 Turbulent Flow and Atmospheric Turbulence

The velocity fluctuation distribution in a turbulent flow was studied by Kolmogorov in 1941 [19] and later applied in the branch of optical waves propagation through turbulence by Tatarsky in 1967 [27]. Briefly, we will consider a laminar flow of a fluid having speed $\boldsymbol{v}$, typical scale L, and kinematic viscosity ν. The flow geometry is very simple and is reported in Fig. 5. In this situation, the fluid dynamics states that when the Reynolds number of the flow is larger then 10^3 the flow becomes turbulent. The fluid Reynolds number is defined as

$$R_\mathrm{e} = \boldsymbol{v}L/\nu$$

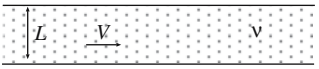

Fig. 5. A sketch of the laminar flow introducing the symbols needed in the following analysis

To understand better the meanings of the R_e number we can write it in the following way:

$$R_e = (v^3/L)/(v^2/L^2\nu) \tag{6}$$

Now we note that the numerator and denominator of the above fraction represent the kinetic energy per unit time and mass and the energy dissipated by viscous friction (per unit time and mass). So it is understandable then when the dissipated energy is much less than the energy received by the fluid (per unit of time and mass) the laminar regime breaks down and we enter the turbulent regime. This is always the case for the free atmosphere were the kinematic viscosity value is $1.5 \times 10^{-7}[\mathrm{m^2 s^{-1}}]$. Substituting this value in the Reynolds number expression, we find that even a wind speed of $1\,\mathrm{ms}^{-1}$ will generate a Reynolds number of the order of 10^6 giving rise to a fully developed turbulent flow. As already mentioned, it was Kolmogorov who devised a simple but effective approach to the description of the velocity fluctuation in a turbulent flow. The Kolmogorov theory is usually called the vortexes cascade from the simple concept that is the theory basis. This concept is explained in Fig. 6, where the vortexes cascade is graphically illustrated together with the relevant quantities of the process. Briefly, we start with the turbulent flow generating vortexes on a scale equal to the laminar flow initial scale L. This scale is usually called the outer scale of turbulence.

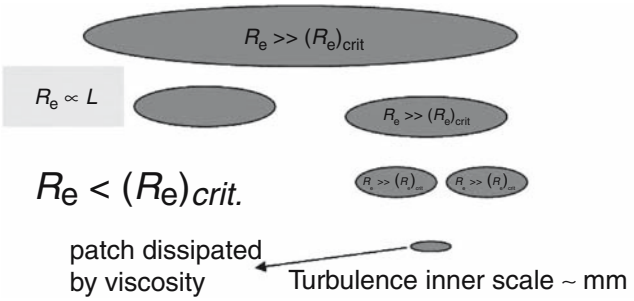

Fig. 6. Graphical representation of the vortex cascades. The turbulent flow generates a vortex of linear dimension L (*outer scale*).The Reynolds number R_e of this vortex is greater than the critical one $(R_e)_{\mathrm{crit.}}$ and the vortex is split into another vortex of a smaller linear dimension. If this vortex still has $R_e >> (R_e)_{\mathrm{crit.}}$, the process is iterated, generating the vortex cascade. The cascade stops when the the vortex energy is dissipated by viscosity. The linear dimension of the smallest vortex is called *inner scale*

These vortexes will have some velocity fluctuation and will have a Reynolds number greater than the critical one. As a result of this condition, they vortexes will split in to other vortexes having a smaller scale and other velocity fluctuations. This process will stop when the small vortexes have a Reynolds number lower then the critical one. At this point, they will be dissipated by viscous friction in the fluid and will not split anymore. The spatial scale where this happens is called the turbulence inner scale and is of the order of a few mm. Using dimensional consideration and the above given description of the turbulence regime, Kolmogorov was able to express the so-called structure function of the velocity fluctuations that we report below

$$D_v(r) = C_v^2 r^{2/3}, \tag{7}$$

where r is the distance between the two considered points, and C_v^2 is a constant that accounts for the strength of the velocity fluctuations.[3] Tatarsky applied this expression in the computation of the phase perturbation experienced by an electromagnetic wave propagating in an inhomogeneous medium (a medium where the refraction index is not constant in space), introducing the concept of a physical quantity that is a conserved passive additive [27]. The relevant example is the atmospheric temperature. This quantity does not change in any way the fluid dynamics, and its values are not modified by atmospheric turbulence. For example, a colored dye added to a turbulent flux would be a passive conserved additive and would be useful for tracing the velocity fluctuations. Tatarsky demonstrates that the fluctuation distributions of any such quantity in a turbulent flow are described by the same structure function of the velocity fluctuations. Using this result, he described the temperature fluctuation in the turbulent atmosphere by the following structure function

$$D_{\mathrm{T}}(r) = C_{\mathrm{T}}^2 r^{2/3}, \tag{8}$$

where r is the distance of the two considered points, and C_{T}^2 is a constant accounting for the strength of the temperature fluctuations. The next step in Tatarsky's work is to consider the expression of the atmospheric refraction index as a function of pressure P and temperature T. This common expression is reported below for easy reading.

$$n = 1 + 10^{-6} \times 79 \left(1 + \frac{7.5 \times 10^{-3}}{\lambda^2}\right) \frac{P}{T} \tag{9}$$

From this equation, it is easy to find out the expression of refraction index fluctuation as a function of temperature. In the following, we will neglect the fluctuations due to pressure changes because pressure fluctuations are usually

[3] We report here the mathematical definition of the structure function $D_x(\rho)$ of a random function $xD_x(\rho) = \langle (x(r+\rho) - x(r))^2 \rangle$. The quantities r and ρ can be one, two, or three dimensional quantities. The last case is the case of the velocity fluctuation structure function.

much less in percentage than the temperature fluctuations. With this in mind we find that

$$\mathrm{d}n = -79\frac{P}{T^2}10^{-6}\mathrm{d}t \tag{10}$$

Combining (8) and (10) we find the expression for the refraction index fluctuation structure function reported below

$$D_n(r) = C_n^2 r^{2/3} \tag{11}$$

In this formula, the quantity C_n^2 is called the constant of refraction index fluctuations structure function and is a measurement of the strength of the atmospheric turbulence in the considered conditions.

3.2 The Phase Structure Function

To compute the phase perturbation experienced by a plane wave propagating through a medium with refraction index fluctuations expressed by (11), we will considered the geometry given in Fig. 7.

Even in this case, the phase fluctuations will be described using a structure function but the phase structure function is given as a two-dimensional function instead of a three-dimensional function (used for the refraction index structure function). In particular, the phase structure function measures the phase difference between two points at distance ρ when both points are located in a single plane perpendicular to the propagation direction of the considered plane wave. This plane is usually taken as containing the telescope

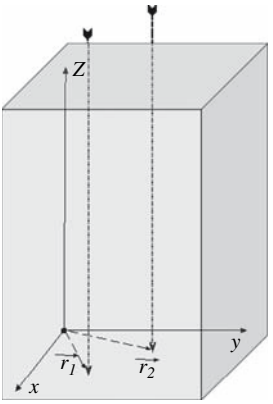

Fig. 7. The geometry used to compute the phase structure function. The grey volume represents the turbulent atmosphere. The integral in (12) is done along the vertical lines showed in the picture. The bottom plane represents the telescope entrance pupil plane

entrance pupil. Considering that the expression of the phase $\phi(r)$ in the plane x,y of the figure is given by

$$\phi(\boldsymbol{r}) = \frac{2\pi}{\lambda} \int_0^{+\infty} n(\boldsymbol{r}, z)\mathrm{d}z \tag{12}$$

then the phase structure function is defined as

$$D_\phi(\rho) = \left\langle [\phi(\boldsymbol{\rho}) - \phi(\boldsymbol{\rho} + \boldsymbol{r})]^2 \right\rangle \tag{13}$$

The analytical expression for the phase structure function was found by Fried in 1965 [10] and is given by

$$D_\phi(r) = 6.88(r/r_0)^{5/3} \tag{14}$$

In this equation, the quantity r_0 is the so-called Fried parameter that is defined as follows, where λ and γ are the considered wavelength and the line of sight zenith angle.

$$r_0 = 0.566\lambda^{6/5} \cos(\gamma) \left[\int_0^h C_n^2(h)\mathrm{d}h \right]^{-3/5} \tag{15}$$

An interesting thing can be inferred from looking at (14). It is easy to see from here and from the r_0 definition that the phase fluctuation is inversely proportional to the considered wavelength so that the optical path defined as the phase fluctuation times the wavelength is achromatic. This result is quite important in the study of the AO systems.[4]

3.3 The Taylor Hypothesis of Frozen Turbulence

The theory considered so far gives the description of the spatial distribution of the phase fluctuations at the telescope entrance pupil in a turbulent atmosphere. However, until now we have not taken into account the dynamic evolution of such a pattern. A simple model describing the dynamics of the turbulence that is usually applied in the case of AO system computations is called the Taylor model [28]. This model makes two assumptions:

- the refraction index fluctuation distribution is constant with time
- the fluctuation distribution is translated on the telescope aperture by the wind

From this model, the turbulence evolution can be derived by simply translating the phase perturbation over the telescope aperture, at the speed of

[4] This result is due to the fact that we neglect the wavelength dependance in (9). and is usually allowed because at optical wavelength the neglected term accounts for some percentage of the optical path difference fluctuation.

wind. The basis of the Taylor model can be identified considering the previous discussion on the Kolmogorov theory of vortex cascade. Let us consider again the case of fully developed turbulence. In this case, the energy per unit of time and volume of a given velocity fluctuation is given by $E_l = (v_l)^2$. Then, as seen already, the energy dissipated by viscous friction at the scale l per unit of time and volume is $\left[(v_l)^2/l^2\right]\nu$. Taking the ratio of these two quantities gives the lifetime of a velocity fluctuation of scale l. Numerically we find

$$\tau_l = l^2/\nu \tag{16}$$

This expression shows that the lifetime is smaller for smaller inhomogeneity. In particular, a quadratic law relates the size of the inhomogeneities and their lifetime. So, if we compute the lifetime for inhomogeneities having linear dimension r_0 we find $\tau_{\min} = 25$[s]. This time is actually much larger than the time taken for a given phase perturbation pattern to pass over a telescope having a diameter of 10 m, even with a very moderate wind of some meters per second. Hence, the pattern can be considered stable and the Taylor hypothesis holds. At this point, it is easy to estimate the characteristic time of the turbulence evolution that results

$$\tau_{\text{atm}} \simeq r_0/v_{\text{wind}} \tag{17}$$

More precise computations of this quantities gives a value of

$$\tau_{\text{atm}} = 0.32 r_0/v_{\text{wind}}$$

We refer the reader to the Beckers [2] paper for a detailed description of this parameter.

4 Effect of Atmospheric Turbulence on the Long Exposure PSF

It is important to be able to determine the telescope MTF when atmospheric perturbations are present. In other words, we want to compute the MTF of a telescope looking through the turbulent atmosphere. In the astronomical case, the exposure time is usually much longer than the atmospheric correlation time; thus, the relevant MTF is the time-averaged MTF. Assuming ergodicity conditions, we will substitute the time average with a statistic average. For this computation, we will have to use the phase structure function defined already. The results reported in this section have been obtained by Fried in 1966 [11]. The expression for the MTF in the case of an integration time much longer then the correlation time of refraction index fluctuations is given by

$$\langle \text{MTF}(f) \rangle \propto \left\langle \int W(\boldsymbol{r}+\boldsymbol{d}) W(\boldsymbol{r}) \mathrm{d}\boldsymbol{r} \right\rangle = \int P(\boldsymbol{r}+\boldsymbol{d}) P(\boldsymbol{r}) \mathrm{d}\boldsymbol{r} \left\langle \mathrm{e}^{(\phi(\boldsymbol{r}+\boldsymbol{d})-\phi(\boldsymbol{r}))} \right\rangle, \tag{18}$$

where $\langle and \rangle$ represent the expectation value of the given quantity a. Now, considering the central limit theorem the above expression can be rewritten as

$$\langle \mathrm{MTF}(f) \rangle \propto T_0(d/\lambda) \cdot \mathrm{e}^{-0.5 D_\phi(d)} \tag{19}$$

In this way, the system MTF has been written as the product of the unperturbed telescope MTF T_0, already reported in Fig. 4 and a damping factor that depends exponentially on the phase structure function which in turn is a function of the Fried parameter or of the turbulence strength. In Fig. 8, we report some cases of MTF for a D/r_0 value of 30, 20, and 10. These are typical cases for an 8 m telescope at visible and NIR wavelengths, respectively. In the picture, we assume that the atmosphere is corrected using an AO system with 30 actuators on the telescope diameter. The assumption is made here that all the wavefront perturbations of scale larger then the actuator pitch of $d_{\mathrm{act}} = D/30$ are perfectly corrected. This is reflected in the behavior of the structure functions that saturate for distances larger then d_{act}. The left side picture is reporting the structure function values for the uncorrected and corrected cases as a function of the different values of D/r_0. On the right side picture we report the corresponding MTF computed using (19).

5 AO System Fundamental Parameters

In this section, we will describe the main parameters of an AO system, in order to give an estimate of the AO systems' current performances and limitations.

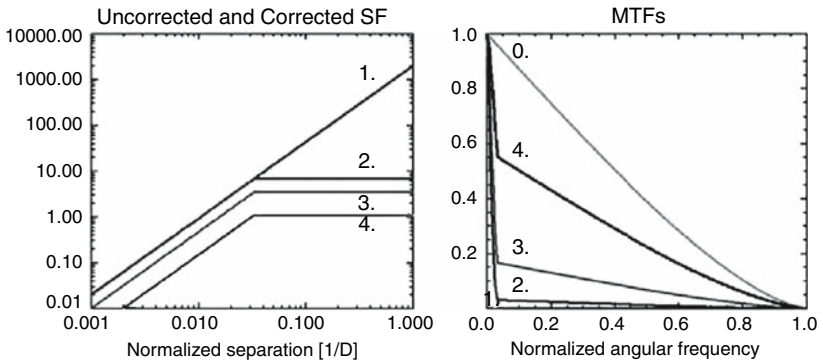

Fig. 8. The left part of the figure reports the corrected phase structure functions for the cases $D/r_0 = 30, 20, 10$ (2., 3., and 4. respectively), together with the uncorrected one (1.). The effect of the wavefront correction is clearly visible in the saturation of the structure functions. The right side reports the corresponding MTFs computed from (19), with the diffraction limited MTF as reference (0.)

In Fig. 1, the basic layout of an AO system is reported to clarify where the relevant parameters come into play. We start by looking at the picture from the deformable mirror, going in a counterclockwise direction.

5.1 Number of Actuators and System Cycle Time

The relevant parameter for the deformable mirror is the number of degrees of freedom, usually given by the number of actuators. The aim of this device is to introduce in the incoming wavefront an optical path difference equal and opposite to the perturbation induced by the atmosphere at a given time. The sum of the two perturbations will give as a result a plane wave. As mentioned, the spatial scale of the atmospheric perturbation is given by the r_0 value. Hence, in order to have the proper resolution on the corrective device, we need to have an actuator grid with pitch smaller then r_0. In this case, the total number of actuators can be estimated to be of the order of $(D/r_0)^2$. The second parameter considered is the time required to compute and apply the correction. As we find in Sect. 3.3, the correlation time of the atmosphere is given in the Taylor hypothesis as $\tau \simeq r_0/v$, where v is the considered wind velocity. To be able to apply an efficient correction, the cycle time of the system has to be smaller than τ so that we can write $t_{\text{cicle}} < r_0/v$.

5.2 Wavefront Perturbation Spatial Sampling

Let us consider now the spatial sampling required to properly measure the wavefront aberration. As stated previously, the characteristic length of the atmospheric perturbation is given by r_0. Assuming this, the wavefront spatial sampling has to be of the order of r_0. A commonly used wavefront sensor in AO system is the so-called Shack-Hartmann sensor [20] which uses a lenslet array to obtain the wavefront slopes in several patches of the telescope entrance pupil. A sketch of the sensor is reported in Fig. 9. This will help the reader to have a better understanding of the basic parameter involved in the following calculations. As shown in the above picture, the lenslet array is optically conjugated to the telescope exit pupil. The array has a number of lenslets of the order of $(D/r_0)^2$. Each of the spots produced by the lenslet array is focused on a CCD detector. The intensity pattern of each spot is recorded for any given wavefront measurement. The spot displacement with respect to the zero or to the unperturbed position is measured by computing the intensity of center of gravity

$$x_{\text{c}} = \sum_{i=1}^{N} I_i x_i / \sum_{i=1}^{N} I_i \tag{20}$$

where I_i and x_i are the intensity and the position of the i-th pixel considered. Moreover it is easy to show in geometrical optics approximation that

$$x_c = f_{\text{sh}} \overline{\partial w(x,y)/\partial x}, \tag{21}$$

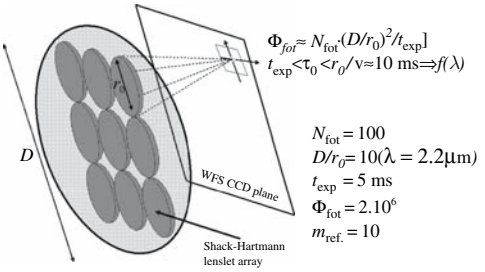

Fig. 9. A simple design of a Shack-Hartmann sensor reporting the basic optical elements of the device. The grey circle is the image of the entrance pupil of the telescope. The single lenslet dimension is chosen to be equal to the scaled length of r_0 on the pupil image

where $w(x, y)$ is the wavefront perturbation and, $f_{\rm sh}$ is the Shack-Hartmann lenslet focal length. The overbar denotes an average of the first derivative over the considered sub-aperture. Thus, the center of gravity is proportional to the wavefront slope in the considered sub-aperture defined by a particular lenslet. The measured data are used to write a linear system of finite difference equations relating the wavefront slopes to the phase difference on the various sub-apertures [12]. This system is usually solved by least square methods. The error in the reconstructed wavefront depends on the total number of photons received by each sub-aperture. This photon number is given by

$$\Phi = N_{\rm fot} \left(D/r_0\right)^2 / t_{\rm exp} \propto r_0^{-3} \tag{22}$$

in order to have 100 photons, per sub-aperture, per integration time[5]. Assuming $D/r_0 = 10$, $t_{\rm exp} = 0.005$, we need an overall flux $\phi = 2e6$ or a star of visual magnitude 10. This number shows that the reference star to be used for wavefront sensing is relatively bright and is not always available in the surroundings of the faint astronomical object we want to observe. Finally, we note that the flux dependance on the third power of r_0 tells that the flux requirements became very strong when the correcting wavelengths got shorter and shorter. A great advantage is usually obtained by performing the wavefront sensing at optical wavelengths and the adaptive correction in the NIR (usually 1–5μm). Doing so, the wavefront sensor can use a visible CCD camera (much faster and less critical than the IR detector). The adaptive correction is done in the J, H, and K bands, where r_0 is larger and the requirements for all the parameters like number of actuators, sub-apertures, and time response, are all relaxed with respect to the visible band. This strategy is allowed

[5] We assume here that 100 photons per sub-aperture per integration time are enough to have a good SNR in the center of gravity measurement. It can be shown that the accuracy in this measurement is given by $\delta x_{\rm c} = \theta/\sqrt{N}$, where θ and N are the lenslet spot full width half maximum and the received number of photons.

by the achromaticity of the optical path, as demonstrated in Sect. 3.2. This means that the correction done by the adaptive mirror, driven by an optical wavefront sensor, is valid for all the wavelengths. An adaptive Optics system working in this configuration is called polychromatic AO system. Finally, it is important to stress that for a polychromatic system the r_0 we referred to above estimating the number of actuators and the number of sub-apertures is computed at the correcting wavelength (in the NIR).

5.3 Reference Source and its Angular Distance from the Scientific Object

The main effect that limits the usefulness of an AO system as described up to now is the so-called angular anisoplanatism. The angular anisoplanatism issue was analyzed by Fried [13] and later by other authors. We have already mentioned that because the reference star has to be considerably bright, the scientific target is rarely used as a reference star. Instead, a closely positioned star of high enough magnitude is used. To see how close the reference star has to be, we consider Fig. 10. In the figure, the telescope entrance pupil and a single turbulent layer are represented. As clearly shown, the two rays crossing the same point of the entrance pupil and coming from the scientific and reference objects, respectively, do cross the turbulent layer in two different points. In the sketch (Fig. 10), the reference source is located at an angular distance $\theta = r_0/h$ from the on-axis scientific target. The phase perturbations relevant to our discussion are also shown in Fig. 10 . In particular, Φ_1 is

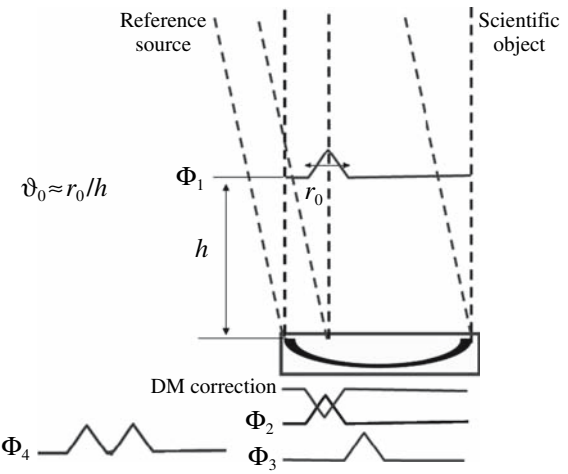

Fig. 10. The figure reports the geometrical arrangement to quantify the wavefront sensing error due to the angular distance between the reference source and the scientific target. The Φ_i are the different phase perturbations involved in the discussion in the text

the phase perturbation on the considered layer at high h; Φ_2 is the phase perturbation experienced by the scientific object placed on-axis, while Φ_3 is the one experienced by the off-axis reference star. The DM is driven to introduce the correction following the phase peak of Φ_3. The result of this correction is represented as Φ_4. This error is called named it such angular anisoplanatism, after Fried [13]: Now we have found as a coherence distance of the atmospheric perturbation the Fried parameter r_0. With this in mind, it is easy to realize that the maximum angle θ allowed between the reference and the scientific object is given by

$$\theta \simeq r_0/h \tag{23}$$

this particular value of θ called isoplanatic angle and is usually indicated as θ_0. The effect of angular separation between reference and scientific target is illustrated in Fig. 23. Substituting real values for r_0 and h, like 0.2 m and 10 km, we find $\theta = 4$ arcsec. This angle is quite small and usually does not allow us to find the 10 mag star we need. It is exactly this problem that limits the sky coverage of an adaptive optics system or the fraction of sky that can be observed efficiently.

5.4 An Estimate of the AO Systems Sky Coverage

The sky coverage (SC) is defined as the percentage of the sky that can be observed using the AO system. This sky fraction is given by: $SC = \pi\theta_0^2 \cdot N^*_{m_0}/4\pi$, where θ_0 is the isoplanatic angle, $N^*_{m_0}$ is the number of stars having magnitude $m < m_0$. Finally m_0 is the AO system limiting magnitude identified using (27). Computing the SC requires a model for the star density as a function of the celestial coordinates. We summarize here all the equations obtained in previous sections and used to quantify the actual sky coverage of an AO system. The formulae we identified are:

$$N_{\text{act}} = (D/r_0)^2 \tag{24}$$

$$\tau_0 \simeq r_0/v \tag{25}$$

$$N_{\text{sub}} = (D/r_0)^2 \tag{26}$$

$$\Phi_{\text{ref}} = vD^2/r_0^3 \tag{27}$$

$$\theta_0 \simeq r_0/h \tag{28}$$

Combining these basic equations J. Beckers [2] compiled a table that we present in Fig. 11. In this table, the various AO system parameters are identified as a function of the values of r_0, τ_0, and θ_0. Figure lists the sky coverage of the AO system as a function of the correcting wavelength. The sky coverage in the K band is 14% but it goes down to 5% in J band. In the visible wavelength regime the situation gets dramatically worst. This is mainly due to the third power dependance of the needed reference flux from r_0 which in

Limiting V magnitude for polychromatic wavefront sensing and sky coverage at average Galactic latitude for different spectral bands[a]

Spectral band	λ (μm)	r_o (cm)	τ_o (sec)	τ_{det} (sec)	V_{lim}	θ_o (arcsec)	Sky coverage (%)
U	0.365	9.0	.009	.0027	7.4	1.2	1.8 E-5
B	0.44	11.4	.011	.0034	8.2	1.5	6.1 E-5
V	0.55	14.9	.015	.0045	9.0	1.9	2.6 E-4
R	0.70	20.0	.020	.0060	10.0	2.6	0.0013
I	0.90	27.0	.027	.0081	11.0	3.5	0.006
J	1.25	40	.040	.0120	12.2	5.1	0.046
H	1.62	55	.055	.0164	13.3	7.0	0.22
K	2.2	79	.079	.024	14.4	10.1	1.32
L	3.4	133	.133	.040	16.2	17.0	14.5
M	5.0	210	.21	.063	17.7	27.0	71
N	10	500	.50	.150	20.4	64	100

[a] Conditions are: 0.75 arcsec seeing at 0.5 μm; $\tau_{det} = 0.3\ \tau_o = 0.3\ r/V_{wind}$; $V_{wind} = 10$ m/sec; $H = 5000$ meters; photon detection efficiency (includes transmission and QE) = 20%; spectral bandwidth = 300 nm; SNR = 100 per Hartmann-Shack image; detector noise = 5 e^-.

Fig. 11. A table taken from the J. Beckers's review published in 1993 [2]. The situation is now changed due to the use of laser-generated reference stars

turn is almost linearly proportional to $\lambda^{6/5}$. In the V band the sky coverage is of the order of some parts per million. As already mentioned this was the big limitation of the astronomical AO system at the time Beckers was writing. The solution to this problem was proposed in 1985 and is described in the next section.

6 Solving the Sky Coverage Problem: The Artificial Reference Sources

As we have seen, the main limitation of an astronomical AO system, as described till now, is the limited sky coverage. This limit is due to the relatively small number of stars bright enough to be used as a reference source. To solve this problem, in 1985, R. Foy and A. Labeyrie [8] proposed the use of an artificially generated reference star. To generate this kind of source, the authors proposed the use of the resonant backscattering from atoms and molecules in the free atmosphere. A favorable one was the sodium atom. Sodium atoms accumulate at a height of ~90 km.

The resonant backscattering of such atoms can be excited using laser light tuned at the wavelength of 589 nm. This produces photons (which return to the telescope) from a given location in the sky. In addition, the reference source location is determined by the laser pointing direction and can be moved at will, and placing the reference source close to the scientific object solves

the sky coverage problem. This type of laser system is called a laser guide star (LGS) and is now a reality for most 8–10 m class telescopes. It will also be a key issue for the ELTs of the future. However, even if the use of LGSs increase substantially, the resultant SC will still not be the 100% desired by the astronomers. This is due to two effects briefly explained below.

6.1 The Tilt Indetermination Problem

To explain the problem of tilt indetermination in the signal obtained by an artificially generated reference star, let us consider the geometry of the laser launch and measurement. There are several possible geometries for the laser launch. However, the tilt indetermination problem holds, even if in slightly different terms, for all possible launching and measurement geometries. We will consider in our discussion one of the most commonly used geometries, where the laser beam is launched from behind the telescope secondary mirror. This situation is represented in Fig. 12.

The laser beam is focused on the sodium layer at an altitude of 90 kms. The backscattered light is received by the full aperture of the telescope. The

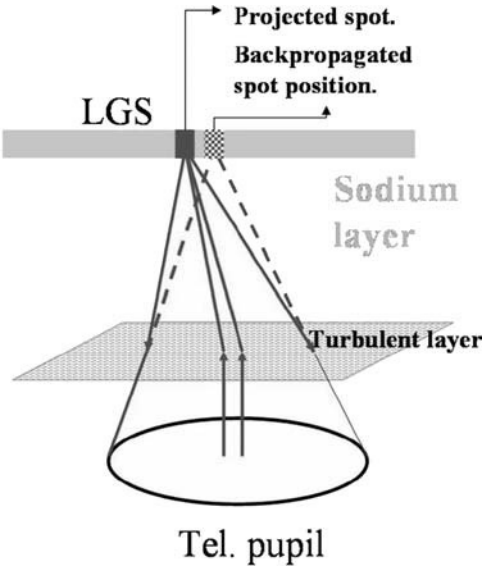

Fig. 12. The above sketch depicts the laser beam launched from the telescope to the Na layer to produce the artificial reference source. During the upcoming path, this beam crosses the turbulent layer, introducing a tilt, which in turn generates a displacement of the artificial star in the sodium layer. In this way, the tilt detected on the LGS is the sum of the tilt experienced by the laser before the LGS generation and the one experienced when the LGS beam is received by the telescope aperture crossing again the turbulent layer

global tilt of the wavefront should be detected as the laser spot displacement in the telescope focal plane. However, the spot displacement measured is due to two different terms. The first one is the tilt that the beam experiences in going up to the 90 km altitude layer. This term is the tilt term due to the tilt perturbation on the scale of the launching telescope, usually of the order of 30–40 cm. The second one is the tilt experienced by the wavefront that propagates from the sodium layer down to the entrance pupil of the telescope. So, the spot displacement is the sum of two tilts and is not a correct measurement of the tilt of a natural guide star that crosses the atmosphere only once. Using the LGS tilt to correct the tilt of the scientific object seriously degrades the telescope angular resolution. To solve this problem several solutions have been proposed [6, 9, 23], but the core solution is to measure the tilt term of the wavefront perturbation using a natural guide star. In this case, we are back to the initial problem of finding a reference star. However, there are two favorable circumstances that mitigate this problem. First, the isoplanatic angle for the tip tilt measurement is larger than the usual isoplanatic angle, allowing a larger sky region to be used for reference star searching. Second, the tilt measurement is made with the full telescope aperture so that the the star magnitude can be fainter than the standard magnitude needed for wavefront sensing described in Sect. 5.2. Overall, the sky coverage for AO systems with a laser guide star is usually improved and ranges between 30% and 90% [26]. These numbers have to be compared with sky coverage values of some percent reported in Fig. 11.

6.2 The Focus Anisoplanatism Problem

There is a second problem that has to be taken into account when a laser guide star is used as a reference star in an AO system. Because the reference source is located at a finite altitude over the telescope, the waves reaching the telescope are spherical. These spherical waves do not sample the same atmospheric volume as the plane wave coming from the star, thus implying that the aberration measured using the laser light is not exactly the same as that experienced by the light of the scientific object. This effect was first studied by Fried [14], who named it focus anisoplanatism, as it arises from a difference in focus of the reference and the scientific object. The geometrical situation is reported in Fig. 13, where a section of two sampled volumes is reported for clarity. As shown in Fig. 13, the perturbations experienced by a ray hitting a given point of the primary mirror are different depending on the ray starting from a source at finite altitude or from a celestial object assumed to be placed at infinity. [It is clear from what we stated in the previous sections that when the distance d, shown in Fig. 13, is larger than r_0, the focus anisoplanatism error becomes significant].

Finally we note that due to the finite altitude some of the turbulence is not sampled at all by the laser light. Following the analysis of this error given by D. Fried, we find that the wavefront error due to this effect can be expressed

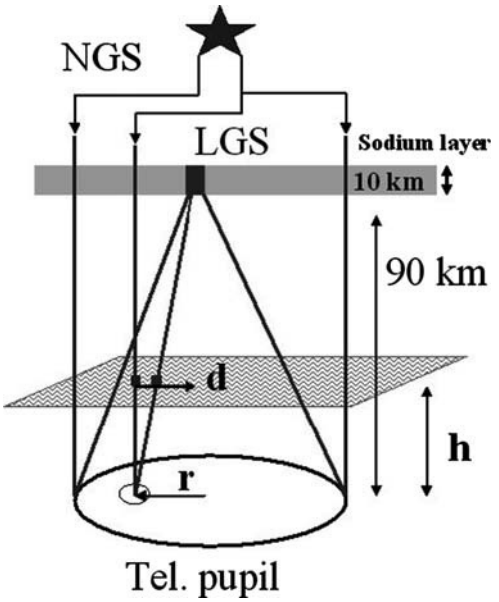

Fig. 13. The above sketch illustrates how the finite altitude of the Na layer affects the wavefront detection. The LGS is seen by the telescope as an object at a finite distance. Due to this, two rays hitting the same telescope pupil point **r**, but coming from the LGS and natural guide star (NGS) respectively, cross the turbulent layer at different points at distance d

by

$$\sigma^2 = (D/d_0)^{5/3}, \tag{29}$$

where d_0 is a parameter that scales with the wavelength as r_0 having quite a complicate expression [14]. The value of this parameter for a standard astronomical site is about 4 m in the infrared. Hence, a single laser guide star can be used to perform AO observations with a focus anisoplanatism error of some radians squared in the near infrared.

7 LBT: An Adaptive Telescope

To show an application of adaptive optics to an 8 m class telescope, we will briefly describe the AO system of the Large Binocular Telescope (LBT). The LBT with AO can be used in single dish or interferometric mode. The LBT is a binocular telescope made up of two 8.4 m primary mirrors. The mirrors are placed on the same mount and can work as two separate units or as an interferometer (the center to center distance of the two primary mirrors is 14 m). A drawing of the telescope is presented in Fig. 14. It is also interesting to

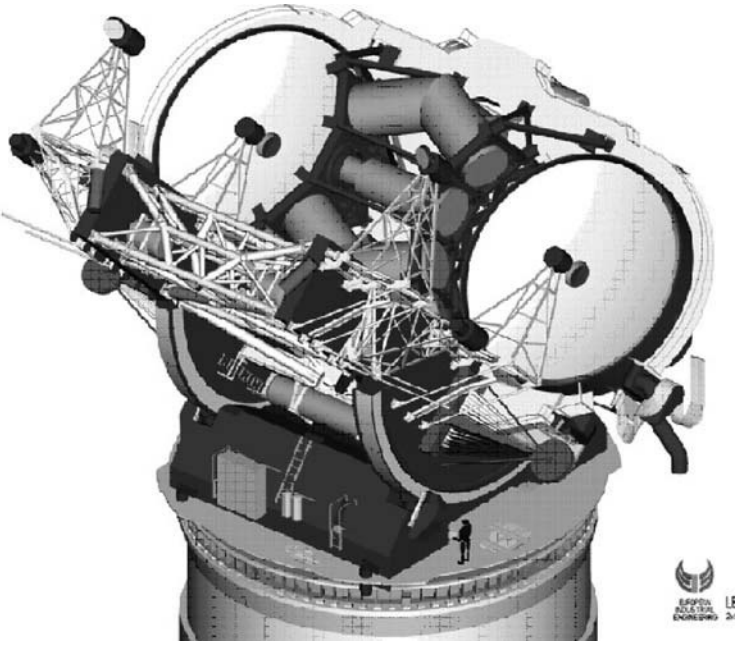

Fig. 14. The Large Binocular Telescope mechanical drawing, showing the two primary mirrors supported by a single mount. Cylinders between the two primary mirrors represents the adaptive intruments of the LBT. From bottom to top they are LUCIFER, LBTI, and NIRVANA

note that LBT is possibly the first 8 m telescope to have an adaptive secondary mirror [24]. In other words, both the secondary mirrors of the LBT will have 672 actuators and can provide adaptive correction for all the telescope focii. We will considered in the following all the instruments that are located at the Bent Gregorian focal stations. Those stations and instruments are represented by the cylinders in Fig. 14.

7.1 LUCIFER: The Single Dish Imager and Spectrograph

We begin our AO system description with LUCIFER[6] [21], the NIR imager and spectrograph placed at the front Bent Gregorian focal station of LBT. This instrument can work in seeing limited or diffraction-limited conditions with a Field of View of 4×4 or 0.5×0.5 arcminutes, respectively (some instrument characteristics, particulary for these modes, are reported in Table 1).

[6] **L**BT NIR spectroscopic **U**tility with **C**amera and **I**ntegral-**F**ield Unit for **E**xtragalactic **R**esearch.

Table 1. Some basic characteristics of LUCIFER's imaging and spectroscopic modes

LUCIFER	
Detector	HAWAII-2 (2048×2048)
Bands	Z J H K
MOS mode	30 position cold mask
Diffr. limited mode	
FoV	0.5×0.5 arcmin
Scale	0.015 arcsec/pixel
Slit length	≤ 0.5 arcmin
R (K)	20600 (0.137 arcsec slit)
R (H)	28200 (0.100 arcsec slit)
R (J)	37100 (0.076 arcsec slit)

In the diffraction limited case, the atmospheric turbulence correction will be provided by the First Light AO system (FLAO). This system is mainly composed of the adaptive secondary mirror [24], a pyramid wavefront sensor [7], and a custom electronic system for the real-time computations. Various numerical simulations [5] were done to assess the performance of LUCIFER when the AO system is in operation.

In Fig. 15, we report some simulation results that quantify the limiting magnitude in the imaging mode. In particular, the plot quantifies the point source magnitude needed in the H band, to achieve a SNR = 3 in 30 min of integration, assuming as main noise the sky background brightness. The H band sky background is assumed to be 13.5 mag per arcsec square. Note that the table contains different curves showing the performance as a function of the angular separation between the scientific object and the reference star magnitude. The diffraction- and seeing-limited cases are reported as straight lines for reference. Finally, the number of pixels used to detect the source is optimized, and the top small table shows that the optimal size of the detection region is of 75 mas. This is about 2.4 times the FWHM of the LBT telescope in the H band or the diameter of the first zero of the diffraction-limited PSF (which contains about 80% of the incoming energy).

It is interesting to note that for very bright reference stars the performances are worst when the reference star is located very close to the scientific object (supposed on axis). This is due to the noise created by the photons from the reference star in the scientific target image. The curves for the on-axis reference star assume that the reference and the scientific object are the same, meaning that there is no noise contribution from the reference source. The number of the considered table can be scaled to give the detection limit in terms of surface brightness assuming a spatial resolution of 75 mas. To scale the achieved results, the magnitudes of the y axis in Fig. 15 have to be subtracted by 5.6 mag. A similar kind of plot has been calculated in the case of the diffraction-limited spectroscopic observation with LUCIFER and are

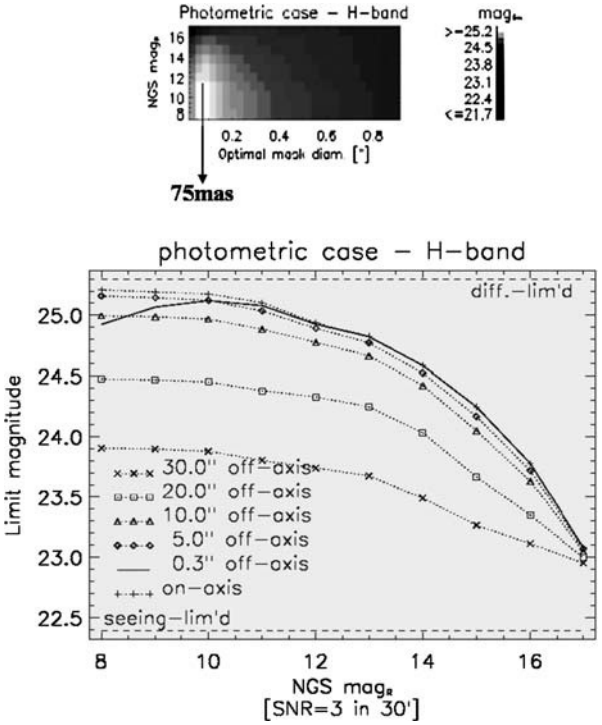

Fig. 15. Bottom: a plot of the limiting magnitude for detection of a point source against the sky background as a function of the reference star magnitude. **Top**: a 2D representation of the optimal window width (x axis) for source detection as a function of reference star magnitude (y axis)

reported in Fig. 16. In this case, the plot quantifies the point source magnitude needed to achieve an SNR = 3 in the H band, in the spectroscopic bin of LUCIFER. The spectral resolution element is 0.06 nm set by the dimension of the slit $\simeq$ 0.1arcsec. Again, the main noise contribution is the sky background brightness assumed to be 13.5 mag. Even in this case, different curves quantify the performance as a function of the relative distance between the scientific object and the reference star. The curves for a diffraction-limited telescope and for a seeing-limited telescope are reported for comparison. The y axis magnitudes can be scaled to evaluate the detection limit for surface brightness [mag/arcsec^2] by subtracting 5.9 magnitudes. Doing so, the plot represents the surface brightness, required to achieve a SNR = 3 in a spectral bin as a function of the NGS magnitude.

7.2 The Adaptive Homothetic Interferometer

At this point, we enter the description of the most challenging part of the LBT operation, the interferometric operations. Before going further, we go

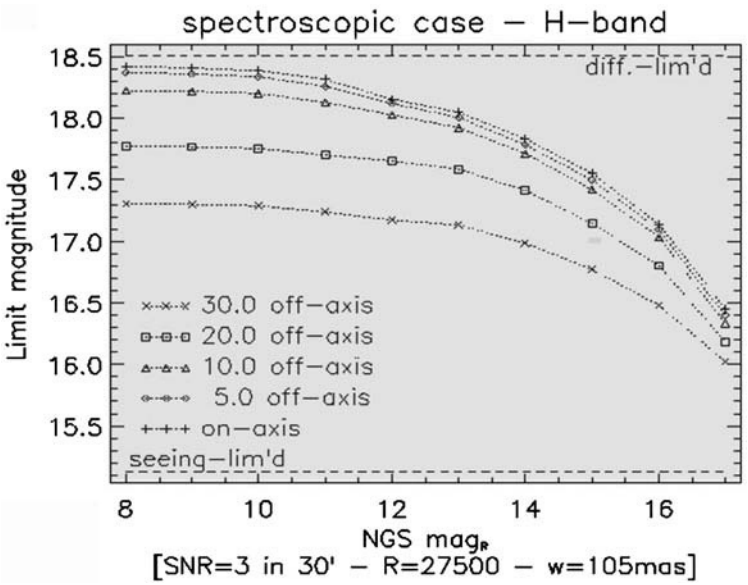

Fig. 16. A plot of the limiting magnitude to reach an SNR of three in the spectroscopic bin (0.06 nm) against the sky background as a function of the reference star magnitude

through some basic concepts of interferometry to explain the definition of a homothetic interferometer. Let us consider a single lens as shown in Fig. 17. The main characteristic of the ideal lens is that the optical path length from surface S to focal point P along each ray of the given wavefront is the same. This condition holds for every direction in the FoV. For this reason, the rays from any object in the FoV arrive at the corresponding focal point in phase

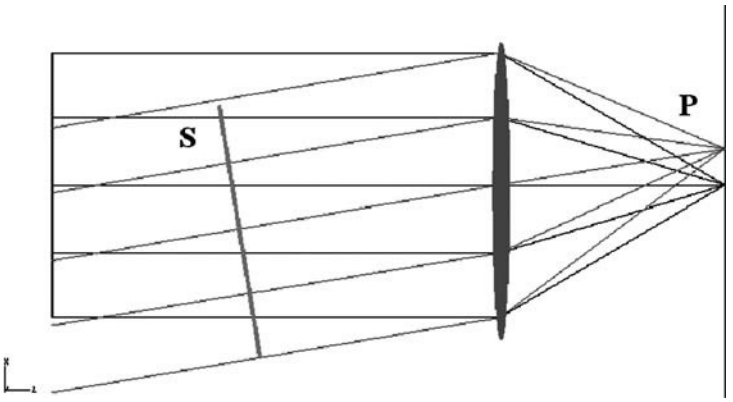

Fig. 17. A figure showing the basic behavior of a lens accordingly to paraxial optics

and positively interfere. The lens glass thickness is calculated to compensate the natural optical path difference of the incoming rays for all the FoV. In this way, all the points located at different positions in the FoV have the same image or, in other words, have the same Point Spread Function, as shown in Fig. 2. Let us consider now the same lens but with a diaphragm covering it. The diaphragm covers the entire lens, except for two small holes of diameter D, placed at a separation b. This separation b is almost equal to the lens diameter (Fig. 18). In this situation, the PSF width is slightly smaller then the initial one (Fig. 19). This is because some portion of the lens having a smaller baseline with respect to the two-holes distance has been rejected. The image we get in the focal plane when $D \ll b$ is usually referred to as Young fringes pattern. In the left picture of Fig. 19, the PSF of a single hole is reported together with the sinusoidal behavior of the interference of the two chief rays from the given sub-apertures. The period of this last curve is λ/b. The final PSF of the system is obtained by considering the two curves and is represented in the right side of the picture. Going off-axis, the Young fringes have a maximum in the location of the image position given by geometrical optics. From a qualitative point of view, this happens because the phase delay between the chief rays of the two sub-apertures is zero. This is due again to the optical path compensation performed by the lens. Finally let us consider now the case of the Michelson stellar interferometer [22] that is represented schematically in Fig. 20. In this case, the light coming from a scientific object is received using two mirrors of diameter D separated by a distance b, with no optical power (M1 and M2 in the sketch). Then, the two beams are reflected and redirected to a mirror with optical power, a lens (L1) in our design, to be focused in the interferometer focal plane.[7] The baseline of this setup is the

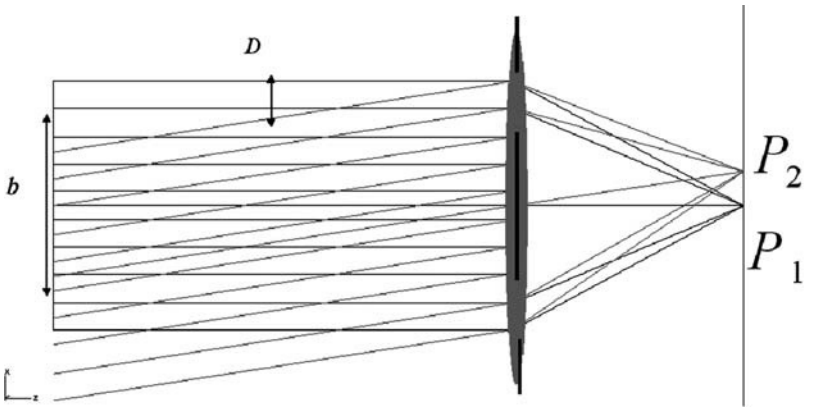

Fig. 18. The optical system made up by a lens and a two-holes diaphragm

[7] Note that the big lens L2 in our representation is shown only to explain the system behavior and is not part of the setup.

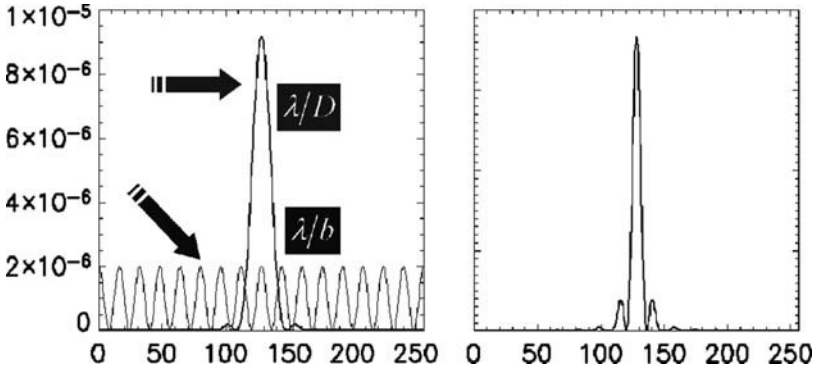

Fig. 19. The elements involved in determining the PSF of the two sub-aperture system. **Left**: The PSF of the single aperture of diameter D superimposed to the sinusoidal behavior of chief ray interference for a couple of apertures spaced by a distance b. **Right**: the two sub-aperture system PSF

distance between the two flat mirrors and can be much larger than the mirrors diameter D, as is presented in the figure. Following the reasoning we did for the two aperture case, we could say that the system PSF should have a width that is much smaller then the PSF of the used mirrors. In particular, the ratio

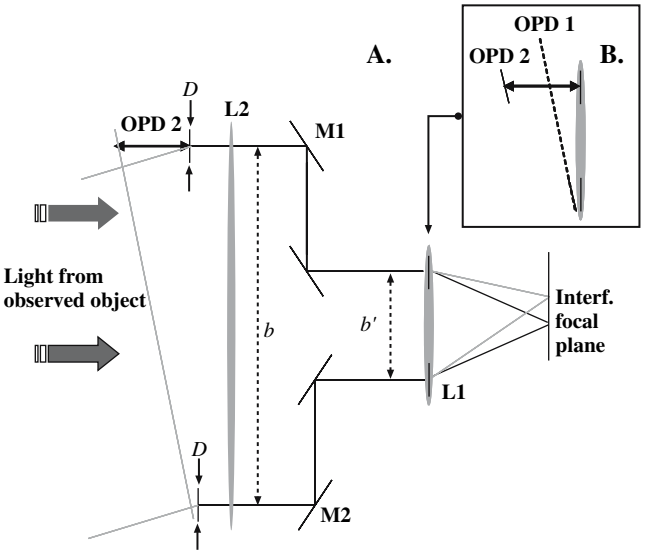

Fig. 20. A schematic representation of the Michelson stellar interferometer. Two sources are represented in the figure to compare the chief rays' behavior for an on-axis object and an off-axis object

between the two PSFs should be D/b. The PSF of this interferometric setup is reported in Fig. 21. The left PSF is achieved for an on-axis object, and the center PSF is achieved for an off-axis object. In both cases, a noticeable gain is achieved in angular resolution because of the small fringe spacings in the PSF. As anticipated, the fringe spacing is a factor D/b smaller then the PSF of the single lens of diameter D (left plot of Fig. 21). It is usual, however, for the PSF shape to change with field of view positions. This means that an image composed of several points will be reimaged through the mentioned system using a different PSF per each point of the FoV. In this case, the image we obtain is no longer a good reproduction of the observed object intensity pattern. Why did this problem not occur with the lens or with the lens and two sub-aperture we described before? As already mentioned, in the lens case the lens glass compensates for the geometrical difference in optical path so that all the rays from a given source arrive in phase at the focal point. In this case, something different happens. A simple idea of the system behavior is found by considering the small inset B in Fig. 20. The two wavefront portions, coming from an off-axis object and sampled by the two mirrors, arrive on the lens with an optical path difference highlighted in the inset by the solid arrow. This is the optical path difference OPD 2, which the big lens L2 would have compensated for, to keep the PSF stable in the field of view. However, the optical path that the lens L1 compensates (at that particular position in the field of view) is different from the one considered above and corresponds to the optical path difference OPD 1 identified by the dashed line.[8] For this reason, the two chief rays from the considered mirrors do not interfere positively in the case of an off-axis source. In other words, the sinusoidal pattern we introduced in Fig. 19 is shifted, with respect to the mirrors PSFs, because of the uncompensated optical path difference. This effect changes the PSF shape with respect to the on-axis case. It is easy to see that this effect is

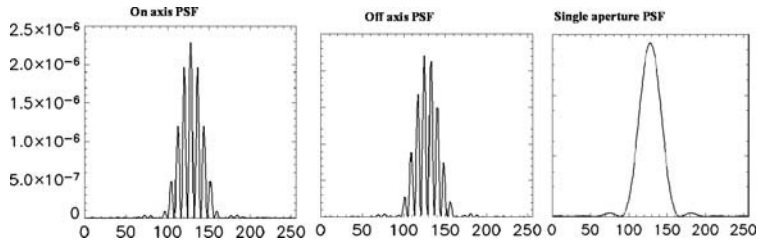

Fig. 21. Left: the on-axis interferometric PSF. The PSF maximum is in the center of the profile. Center: the off-axis PSF. The maximum of the PSF is not in the center of the profile. **Right**: the PSF of the single aperture of diameter D

[8] The dashed line is obtained by considering the wavefront surface perpendicular to the initial propagation direction, identified by the off-axis object position in the sky.

not present on the on-axis object, where for symmetry reasons the sinusoidal pattern remains centered on the mirrors PSF.

Now, what is the difference of the present setup from the lens and the two sub-apertures case we already considered? In this interferometric case, the entrance pupil (the two mirrors of diameter D placed at distance b) is not purely scaled on the re-imaging lens L1. In fact, the mirror diameter remains the same while the mirror separation is scaled from b to b′. This violation to a pure scaling or re-imaging of the entrance pupil of the interferometer generates the optical behavior, where the PSF is not constant with the field of view. An interferometer where the pupil is purely scaled in all the optical train is called homothetic and creates real images of the source. However, no scaling is perfect, and so it is important to understand what is the limit that can be tolerated, when an interferometer is used to produce real images. Let us consider the left picture of Fig. 22, where a homotethic configuration is sketched. Note that the two lenses have been added before the folding mirrors to collimate and compress the beams. In formulae requiring the homotheticity means using the symbols defined in figure:

$$\frac{b}{b'} = \frac{D}{D'} \tag{30}$$

In this case, the chief rays are in phase for all the points of the field of view. Now, suppose that the interferometer aperture is correctly scaled in the plane of the refocusing lens L1 (as shown in the right picture of Fig. 22). However, one of the two apertures is linearly displaced in this plane by an amount ε. Then let us consider the case of a wavefront having a tilt with an OPD amplitude of $N\lambda$ over the interferometric pupil. This is the case of an off-axis object placed at N times the angle λ/b. At the re-imaging lens the wavefront has a slope of $N\lambda/b'$. The displacement of one side of the aperture, the one represented as displaced on the right side in the picture, introduces a phase delay with respect to the perfect case equal to

$$N\lambda/b'\varepsilon$$

as graphically shown in the picture. If we require that the displacement of the sub-aperture does not perturb the image we have to require

$$N\lambda/b'\varepsilon << \lambda \tag{31}$$

or

$$\varepsilon << b'/N \tag{32}$$

This last equation states the precision required in the positioning of the two apertures when the homothetic condition is required on a field of view of $N\lambda b$. In other words, the equation states that the precision in the re-imaging process has to increase as the required field of view. In the LBT case, for example,

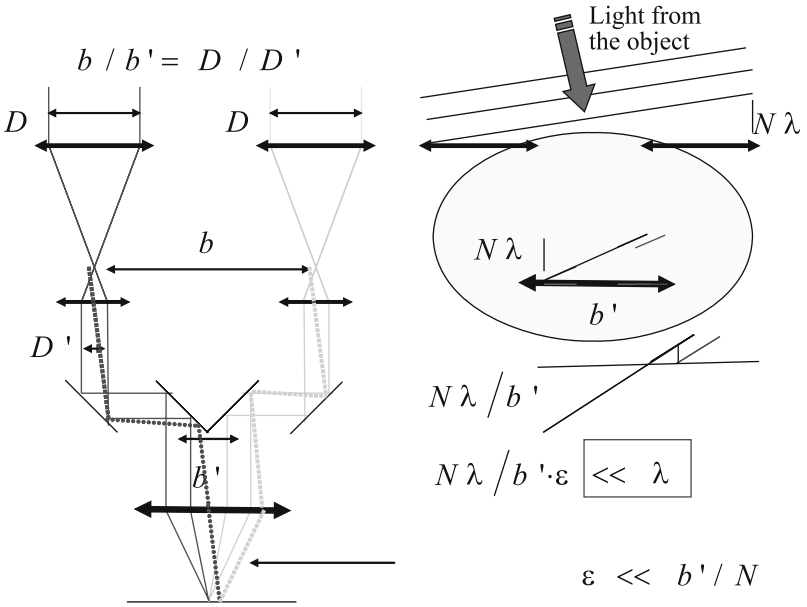

Fig. 22. A figure showing a homothetic interferometer. The right side of the picture is the basic homothetic arrangement while the left picture outlines the main elements used in the homothetic condition computations

the infrared instrument with interferometric capability called NIRVANA has an infrared camera mounted in the interferometric focal plane. Because the field of view of the camera is 15×15s arcsec, and the interferometer resolution λ/b is about 18 milliarcsec, the quantity N is equal to about 750, and b/N is found to be, for a 100 mm pupil spacing on the reimaging optics, equal to 0.13 mm. Requiring that the aperture displacement be much smaller leads to displacements of the order of 0.01 mm or 10 μm. Thus in the pupil re-imaging process the image centering has to have an accuracy of 10 μm. Many other effects can produce the same loss of homotheticity such as, pupil rotations, the pupil magnification, and so on. For all these effects, a similar computation can be done to show what is the limit for a rotation or magnification error when a certain homotheticity is required.

8 Interferometric Instrument at LBT

To complete our description of the adaptive instruments of LBT, we report in this section about the two interferometric instruments of the telescope. Remember that the LBT has two primary mirrors of 8.4 m with a center to center distance of 14 m, achieving the maximum equivalent resolution of a 23 m aperture. The opto-mechanical design of LBT allows one to obtain

a homothetic interferometer in both the interferometric focal stations (top and central cylinders in Fig. 14). All interferometric instruments use adaptive optics to improve performance.

We will start with the European interferometric instrument, briefly mentioned above, called NIRVANA [16]. The instrument objective is to realize interferometric images adaptively corrected on a large field of view (15×15 arcsec). Images are taken in the NIR 1–2.2 μm. The instrument is built in collaboration with the Istituto Nazionale di Astrofisica in Italy, the Max Planck Institute fur Astronomie in Heidelberg, The Max Planck Institute for Radioastronomy in Bohn, and the University of Cologne. The main sub-systems of NIRVANA are the beam combining optics, the Multi Conjugate Adaptive Optics system (MCAO) having four deformable mirrors and six wavefront sensors, the fringe tracker camera to sense the differential piston of the two subapertures, and finally an NIR camera having a field view of 15×15 arcseconds. A drawing of NIRVANA is reported in Fig. 23, where some details of the MCAO sub-systems are visible. The instrument assembly is shown, in the bottom left inset, mounted in the structure of LBT as a large box between the primary mirrors. A simulated image obtained with NIRVANA is presented in Fig. 24. Here a stellar field of 15×15 arcseconds is shown. The particular shape of the PSF with the three central fringes, similar to the PSF we already discussed in the case of the simple lens, is evident. Even in this case, the number of side lobes is due to the ratio between the aperture diameter, 8.25 m, and their separation, 14 m. The interferometric images of LBT taken with the telescope in a given orientation with respect to the celestial coordinates will contain this feature so that the full resolution of the interferometer

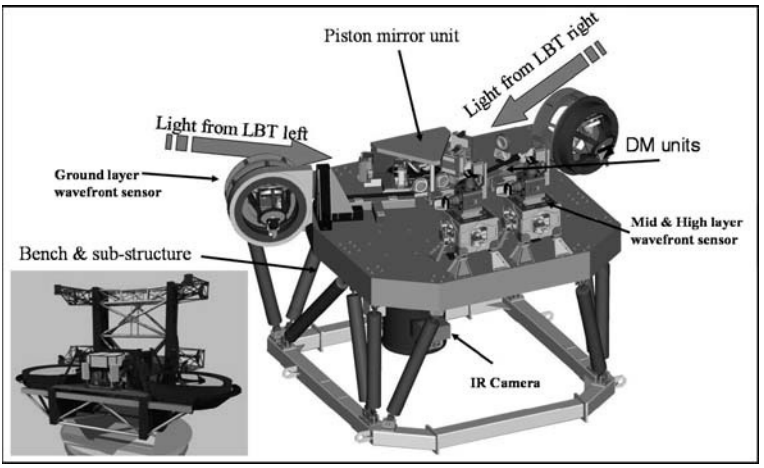

Fig. 23. A drawing of the NIRVANA instrument as mounted in the azimuth platform. The small box in the bottom left corner shows the instrument in the telescope structure, while the large figure shows the main components of the AO system of NIRVANA

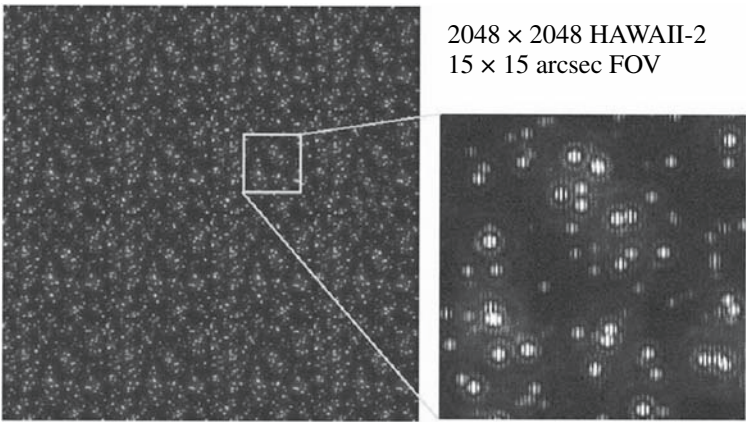

Fig. 24. A simulated image of a 15 × 15 arcsecond stellar field as seen from the LBT interferometric instrument NIRVANA. The three fringes of the interferometric PSF of LBT are clearly visible

is achieved only in the fringe direction. However, taking multiple images with the telescope having the baseline projection in a different orientation with respect to the celestial coordinates will allow the user to have the maximum resolution in all directions. For more details on the image processing due in the NIRVANA case the reader is referred to the [4].

The second interferometric instrument of LBT is the American interferometer called LBTI (*Large Binocular Telescope Interferometer*) [18]. This instrument is realized by the Steward Observatory. In Fig. 25, a mechanical sketch of the instrument is shown. The two input focal planes of LBT telescopes (left and right units) are located close to the top boxes labeled UBC (Universal Beam Combiner). The principal aim of this instrument is to provide sensitive nulling interferometric observations of nearby solar-like stars at $2-20\,\mu$m. In particular, LBTI will be used in collaboration with NASA to perform initial observations for target selection of the U.S. spatial planet finder mission.

The nulling mode uses LBT as a Bracewelll interferometer [3] to produce a dark fringe in the center of the field of view (Fig. 26). This acts as a coronograph allowing masses very close to the central star to be detected. However, to produce a high contrast nulling interferometer, an adaptive optics correction is required. Two AO units will be used, placed at the two interferometric focal stations. The deformable mirrors used will be the adaptive secondary mirrors of the two telescopes. The nulling optics will be placed in the dewar labeled NIL, while the nulling camera called NOMIC will be mounted in the corresponding dewar. The arrangement of such a dewar is reported in Fig. 25. Finally, LBTI is able to provide a beam combination compatible with wide-field homothetic (imaging) interferometry in the thermal infrared 1–30 μm. The imaging cameras for that are indicated in Fig. 25 as Fizeau imagers.

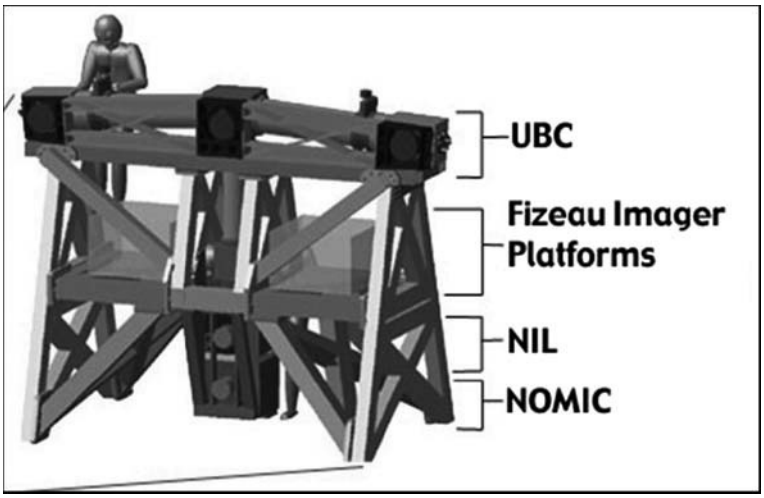

Fig. 25. A sketch of the opto-mechanical arrangement of the LBTI instrument. The left and right side of the structure are close to the two LBT focal planes of the interferometric station

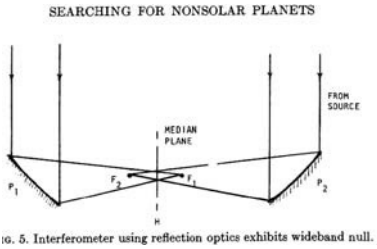

Fig. 26. A sketch of the nulling interferometer principle, where two beams interfere having a phase delay of π. This delay is introduced by using a dedicated optical system

9 Conclusion

The paper has introduced the basic concepts and limitations of modern Astronomical AO systems. The most relevant parameters of such AO systems have been outlined. Using the expression identified for such quantities, the main limitation of Adaptive Optics, namely, the small sky coverage has been analyzed. The present day solution to such a problem, the use of laser guide star, has been described. Then, the diffraction limited instruments that will be operational on the LBT telescope have been introduced. This should provide the reader with an idea of what will be available in the next few years at the LBT telescope in terms of high angular resolution capabilities. Finally, we consider it very important for the astronomers of the next future to

understand performance and limitations of AO systems that today appear to be fundamental to the sub-systems of any 8–10 m class telescopes and the key subsystem of any Extremely Large Telescope presently under design.

Acknowledgments

Some of the figures presented in this paper are taken from available papers and presentations made by the groups developing the instruments LUCIFER, NIRVANA and LBTI. The authors thank all these groups for then contributions.

References

1. Babcock, H.W.: The possibility of compensating astronomical seeing. PASP **65**, pp. 229–236 (1953) 47
2. Beckers, J.M.: Adaptive optics for astronomy – Principles, performance, and applications. Annu. Rev. Astron. Astrophys. **31**, 13–62 (1993). DOI 10.1146/annurev.aa.31.090193.000305 55, 60, 61
3. Bracewell, R.N.: Detecting nonsolar planets by spinning infrared interferometer. Nature **274**, pp. 780–781 (1978) 75
4. Carbillet, M., Correia, S., Boccacci, P., Bertero, M.: Restoration of interferometric images. II. The case-study of the Large Binocular Telescope. Astron. Astrophys. **387**, 744–757 (2002). DOI 10.1051/0004-6361:20020389 75
5. Carbillet, M., Riccardi, A., Femenía, B., Fini, L., Esposito, S.: Preliminary results of simulations for the adaptive optics system of the large binocular telescope. AstroTech Journal, Mem. Soc. Astr. It. **2** (1999) 66
6. Esposito, and, S.: Techniques to solve the tilt indetermination problem: methods, limitations, and errors. In: Bonaccini, D., Tyson, R.K. (eds.) Adaptive Optical System Technologies. Proceedings of the SPIE, vol. 3353, pp. 468–476 (1998) 63
7. Esposito, S., Tozzi, A., Puglisi, A., Fini, L., Stefanini, P., Salinari, P., Gallieni, D., Storm, J.: Development of the first-light AO system for the large binocular telescope. In: Tyson, R.K., Lloyd-Hart, M. (eds.) Astronomical Adaptive Optics Systems and Applications. Proceedings of the SPIE, vol. 5169, pp. 149–158 (2003). DOI 10.1117/12.511503 66
8. Foy, R., Labeyrie, A.: Feasibility of adaptive telescope with laser probe. Astron. Astrophys. **152**, L29–L31 (1985) 61
9. Foy, R., Migus, A., Biraben, F., Grynberg, G., McCullough, P.R., Tallon, M.: The polychromatic artificial sodium star: A new concept for correcting the atmospheric tilt. Astron. Astrophys. Suppl. **111**, 569–578 (1995) 63
10. Fried, D.L.: Statistics of a geometric representation of wavefront distortion. J. Opt. Soc. Am. (1917–1983) **55**, 1427–1435 (1965) 47, 54
11. Fried, D.L.: Optical resolution through a randomly inhomogeneous medium for very long and very short exposures. J. Opt. Soc. Am. (1917–1983) **56**, 1372–1379 (1966) 55
12. Fried, D.L.: Least-square fitting a wave-front distortion estimate to an array of phase-difference measurements. J. Opt. Soc. Am. (1917–1983) **67**, 370–375 (1977) 58

13. Fried, D.L.: Anisoplanatism in adaptive optics. J. Opt. Soc. Am. (1917–1983) **72**, 52–61 (1982) 59, 60
14. Fried, D.L., Belsher, J.F.: Analysis of fundamental limits to artificialguide-star adaptive-optics-system performance for astronomical imaging. J. Opt. Soc. Am. **11**, 277–287 (1994) 63, 64
15. Goodman, J.W.: Introduction to Fourier optics. Introduction to Fourier optics. McGraw-Hill series in electrical and computer engineering; electromagnetics, 2nd ed., McGraw-Hill, New York (1996). ISBN: 0070242542 (1995) 49
16. Herbst, T., Ragazzoni, R., Andersen, D., Boehnhardt, H., Bizenberger, P., Eckart, A., Gaessler, W., Rix, H.W., Rohloff, R.R., Salinari, P., Soci, R., Straubmeier, C., Xu, W.: LINC-NIRVANA: A Fizeau beam combiner for the large binocular telescope. In: Traub, W.A. (ed.) Interferometry for Optical Astronomy II. Proceedings of the SPIE, vol. 4838, pp. 456–465 (2003) 74
17. Hill, J.M., Green, R.F., Slagle, J.H.: The large binocular telescope. In: Stepp, L.M. (ed.) Ground-Based and Airborne Telescopes. Proceedings of the SPIE, vol. 6267, pp. 62670Y (2006). DOI 10.1117/12.669832 47
18. Hinz, P.M., Angel, J.R.P., McCarthy Jr., D.W., Hoffman, W.F., Peng, C.Y.: The large binocular telescope interferometer. In: Traub, W.A. (ed.) Interferometry for Optical Astronomy II. Proceedings of the SPIE, vol. 4838, pp. 108–112 (2003) 75
19. Kolmogorov, A.N.: The local structure of turbulence in incomressible viscous fluids for very large Reynolds numbers. Compt. Rend. Acad. Sci. (SSSR) **30**, 301 (1941) 50
20. Malacara, D.: Optical shop testing. In Malacara, D. Wiley Series in Pure and Applied Optics. Wiley, New York (1992) 57
21. Mandel, H., Appenzeller, I., Bomans, D., Eisenhauer, F., Grimm, B., Herbst, T.M., Hofmann, R., Lehmitz, M., Lemke, R., Lehnert, M., Lenzen, R., Luks, T., Mohr, R., Seifert, W., Thatte, N.A., Weiser, P., Xu, W.: LUCIFER: A NIR spectrograph and imager for the LBT. In: Iye, M., Moorwood, A.F. (eds.) Optical and IR Telescope Instrumentation and Detectors. Proceedings of the SPIE, vol. 4008, pp. 767–777 (2000) 65
22. Michelson, A.A., Pease, F.G.: Measurement of the diameter of alpha Orionis with the interferometer. Astrophys. J. **53**, 249–259 (1921). DOI 10.1086/142603 47, 69
23. Ragazzoni, R.: Propagation delay of a laser beacon as a tool to retrieve absolute tilt measurements. Astrophys. J. **465**, L73–L75 (1996). DOI 10.1086/310139 63
24. Riccardi, A., Brusa, G., Salinari, P., Busoni, S., Lardiere, O., Ranfagni, P., Gallieni, D., Biasi, R., Andrighettoni, M., Miller, S., Mantegazza, P.: Adaptive secondary mirrors for the large binocular telescope. In: Tyson, R.K., Lloyd-Hart, M. (eds.) Astronomical Adaptive Optics Systems and Applications. Proceedings of the SPIE, vol. 5169, pp. 159–168 (2003). DOI 10.1117/12.511374 65, 66
25. Rousset, G., Fontanella, J.C., Kern, P., Gigan, P., Rigaut, F.: First diffraction-limited astronomical images with adaptive optics. Astron. Astrophys. **230**, L29–L32 (1990) 47
26. Sandler, D.G., Stahl, S., Angel, J.R.P., Lloyd-Hart, M., McCarthy, D.: Adaptive optics for diffraction-limited infrared imaging with 8-m telescopes. J. Opt. Soc. Am. **11**, 925–945 (1994) 63
27. Tatarsky, V.I.: Wave Propagation in a Turbulent Atmosphere, p. 548. Nauka, Moskow (1967) 47, 50, 52
28. Taylor, G.I.: The spectrum of turbulence. Proc. R. Soc. Lond. A **164**, 476 (1938) 54